IEEE Access
Multidisciplinary | Rapid Review | Open Access Journal

Received May 25, 2020, accepted July 6, 2020, date of publication July 8, 2020, date of current version July 20, 2020.

Digital Object Identifier 10.1109/ACCESS.2020.3007966

The Authentic 3D Mobility Model Based on Spiral Line for Aerial Backbone Network

DAWEI HE, WEI SUN, (Member, IEEE), AND LEI SHI
Space Science Department, University of Xidian, Xian 710126, China

Corresponding author: Dawei He (252642902@qq.com)

This work was supported in part by the National Nature Science Foundation of China (NSFC) under Grant 61671356.

ABSTRACT For search and rescue (SAR), the dynamic connectivity issue caused by mobility of aerial node will severely influence the actual performance in aerial backbone network (ABN). To capture true aerial mobility feature, some application-oriented aerial mobility model (AMM) has been developed. However, existing 3D AMM cannot satisfy some specific demands for in SAR, especially smooth 3D trajectory and rapid connectivity coverage. In this paper, we propose authentic 3D mobility model based on spiral line (3D SLMM), such as Z-Or-SLMM and Z-Non-SLMM. Firstly, we review the basic concept of 2D SLMM. Then, we develop authentic 3D SLMM based on 2D SLMM. Meanwhile, we validate synthetic trajectory of 3D SLMM through the real traces. In the further, we investigate some mathematical features of 3D SLMM, such as mathematical expression and the distribution of spatial nodes. Finally, we evaluate some key mobility property of 3D SLMM. The result shows that Z-Or-SLMM and Z-Non-SLMM all have specific mathematical expression and uniform distribution of spatial nodes at steady status. Besides, the Z-Or-SLMM and Z-Non-SLMM all possess authentic and smooth 3D trajectory. Specially, the aerial node in Z-Or-SLMM merely takes 1.5 minutes to cover 100% target region of 200m∗200m. We believe that the 3D SLMM can be directly deployed in the actual scene, and provide many helpful and credible guidelines in the design and analysis of realistic ABN.

INDEX TERMS Aerial backbone network, mobility model, smooth trajectory, rapid coverage.

I. INTRODUCTION

In the age of the Internet of everything, the novel 5G technique (e.g. MMW [1], [2], D2D [3]–[5]) can bring various possibilities to urban rescue [6], [35], [36]. In the event of a disaster, the temporary connectivity should be provided to victims through the aerial backbone network (ABN) organized by many aerial nodes [7], [31]. As first and foremost step, the aerial node should rapidly cover whole disaster area to search and rescue (SAR) each victim [32]–[34]. In fact, the actual coverage efficiency may be influenced by some inevitable factors (e.g. environment or radio interference), such that the performance of ABN will be largely decreased [9]. Hence, reliable ABN is required for SAR [8], [29].

Compared with the fixed wing, the rotary wing UAV which can be deployed flexibly and conveniently become an eligible choice to perform SAR [10], [11]. Due to mechanical and aerodynamic constrain, the rotary wing UAV should maintain sufficient space-time correlation during entire flight (i.e. smooth 3D trajectory) [12], [13], [30]. Certainly, the special mobility of UAV will cause dynamic connectivity issue (e.g. connection break [38], delay jitter [39], [40]), thereby severely influence the property of ABN, especially routing protocol [14]–[16]. Therefore, the realistic aerial mobility model (AMM) should be developed [17].

In the preliminary stage, some random mobility model (RMM) has been proposed to simulate movement of human or vehicle (e.g. RW [18], RWP [19], [20] and RD [21]–[23]). Regretfully, these RMM cannot model aerial trajectory because of the sharp change of direction [17]. As advanced version, the GM introduced quite limited space-time correlation also cannot guarantee the smoothness of trajectory [24], [25]. Except RMM, some AMM has been presented for the specific application. As a typical example, the aerial node can transport the cargo according to the plan of flight (FP) [26]. In addition, the DPR [27] and ST model [28] has been developed to imitate the aerial node

The associate editor coordinating the review of this manuscript and approving it for publication was Longxiang Gao.

This work is licensed under a Creative Commons Attribution 4.0 License. For more information, see https://creativecommons.org/licenses/by/4.0/

in the mission of supervision. Besides, the aerial node in the SRCM could search entire disaster area to rescue victim [8]. In previous work, we proposed SLMM for SAR in which the aerial node can rapidly cover whole target region with smooth trajectory [29].

However, most AMM merely concern aerial mobility restricted into the 2D space, such that the research work of AMM related to actual 3D scenario is quite limited. In addition, existing 3D AMM cannot meet the specific demands of SAR without smooth 3D trajectory and rapid connectivity coverage.

In this paper, we develop authentic 3D SLMM in which the aerial node using smooth 3D trajectory can uniformly and rapidly cover whole target region. Firstly, we outline the basic concept of 2D SLMM, as the necessary theoretical cornerstone. Then, we develop authentic 3D SLMM based on SLMM, such as Z-Orthogonal SLMM (Z-Or-SLMM) and Z-Non-orthogonal SLMM (Z-Non-SLMM). Meanwhile, we propose novel flexible boundary model (FBM) to cope with some special situations in SAR. In the further, we investigate some mathematical features of 3D SLMM (e.g. mathematical expression, the distribution of spatial nodes). Meanwhile, we propose a novel method of front and top view (FTV) to validate the analytical result of 3D SLMM. The result shows that the Z-Or-SLMM and Z-Non-SLMM all possess uniform distribution of spatial node at steady status. Moreover, we study some key mobility features of 3D SLMM. The simulation shows that the Z-Or-SLMM and Z-Non-SLMM all have smooth 3D trajectory. Besides, the aerial node in the Z-Or-SLMM can rapidly cover whole target area, compared with other 3D mobility model. In addition, we find that the FBM can flexibly and effectively restrict 3D trajectory of aerial node according to actual requirements.

To the best of our knowledge, the 3D SLMM, as our main contribution, is first and authentic 3D AMM for SAR. In addition, the FBM is first and reliable 3D boundary model to deal with the special situation in SAR (e.g. scramble or limited scene). Besides, the FTV is first and valid method to validate the distribution of spatial node of 3D mobility model. In short, we believe that the 3D SLMM, as a crucial supplement of 3D AMM, can be directly deployed in the actual scene, and provide many useful and credible guidelines in the design and analysis of realistic ABN.

The rest of this paper is organized as follows. In Section II, we review some related works. Then, we outline the concept of 2D SLMM in Section III. In Section IV, we develop authentic 3D SLMM based on 2D SLMM. In the further, we investigate some mathematical features of 3D SLMM in Section V. Then, we discuss some key mobility properties of 3D SLMM in Section VI. Finally, the conclusion and future work is provided in Section VII.

II. RELATED WORKS

In this section, we review some related works to investigate whether existing 3D AMM can satisfy specific demands for SAR, especially smooth 3D trajectory and rapid connectivity coverage.

As the extended version, the aerial node in 3D RWP can randomly select any way points within entire 3D space [41], [42]. Obviously, its trajectory is quite simple (See Figure 1), so that it just imitates macro mobility feature in wide scene (e.g. aviation). Due to the change of sharp direction, the aerial node in 3D RWP cannot capture micro mobility feature in actual scene (e.g. smooth 3D trajectory). With the random altitude, the aerial node in 3D RWP cannot provide rapid and reliable connectivity coverage to the device on the ground. Hence, the 3D RWP is not eligible for SAR. Similarly, the FP also is unreal for SAR, which possesses the same mechanism in essence [26].

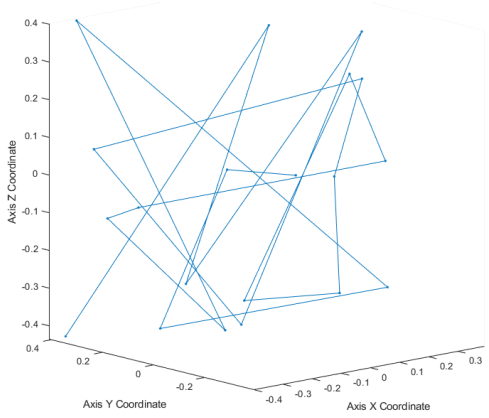

FIGURE 1. The trajectory of 3D RWP.

In [43], 3D mix model (3D MM) is proposed to study 3D mobility feature of aerial node (e.g. covering probability). In fact, the 3D MM is combination between RWP and RW, thereby it still cannot overcome the inherent weakness of RMM. Hence, 3D MM is not suitable for SAR.

Except above 3D RMM, some application-oriented 3D AMM has been developed.

To capture true mobility in surveillance, the aerial node in 3D GM can select speed and direction according to the Markov chain (See Figure 2) [24], [44]. Compared with other 3D RMM, 3D GM has more space-time correlation. But quite limited space-time correlation in 3D GM still cannot guarantee smooth 3D trajectory during flight. On the other hand, stable connectivity coverage could be ensured at a certain degree due to continuous change of altitude. Hence, 3D GM also is not credible for SAR.

Similarly, the comprehensive 3D AMM called 3D ST has been presented [12], [13], such as Z-Independent ST (See Figure 3) and Z-dependent ST (See Figure 4). The 3D ST can capture real mobility feature at turning moment, thereby partly guarantee smoothness of 3D trajectory. Meanwhile, the selection of continuous altitude, which is an important foundation for covering rapidly, can be provided in 3D ST. However, some inherent defects of 2D ST are still inherited into 3D ST (e.g. the change of sharp

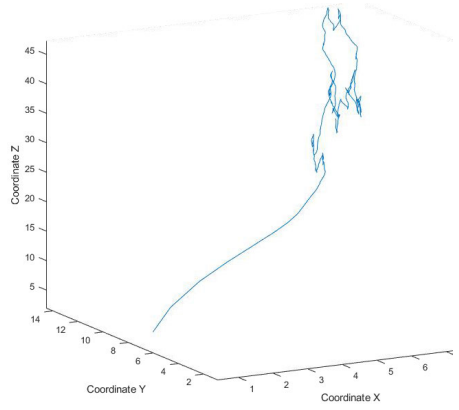

FIGURE 2. The trajectory of 3D GM.

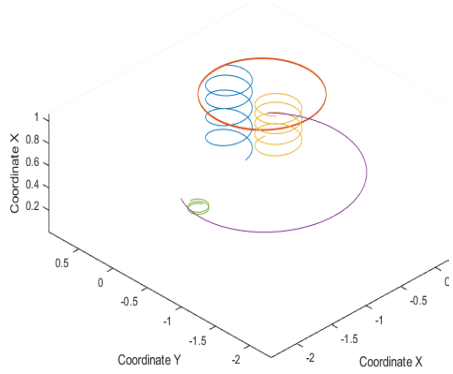

FIGURE 3. The trajectory of Z-Independent ST.

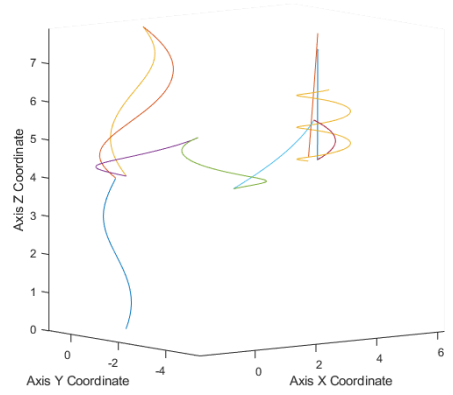

FIGURE 4. The trajectory of Z-Dependent ST.

direction at adjacent interval (See Figure 5)). Without smooth 3D trajectory, 3D ST also is not reasonable for SAR.

In the next section, we will outline the concept of 2D SLMM, as necessary theoretical cornerstone developed the 3D SLMM.

III. THE BASIC 2D SLMM

In this section, we will outline the basic concept of 2D SLMM. Firstly, we elaborate mechanism of 2D SLMM.

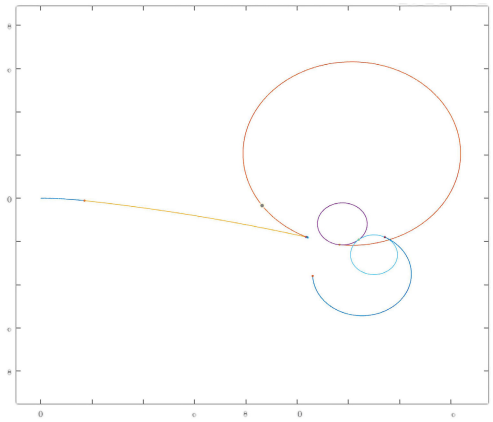

FIGURE 5. The trajectory of 2D ST.

Then, we introduce the annular boundary model (ABM) in 2D SLMM.

A. THE MECHANISM OF 2D SLMM

To imitate realistic aerial mobility, we present some mobility hypothesis in 2D SLMM. Firstly, we utilize angular speed to reflect the speed of aerial node, and assumed that it is the uniform distribution within the certain range. Then, the moving time interval is the exponential distribution with certain coefficient, and the pausing time interval is the uniform distribution within the certain range. In addition, the thread pitch of spiral line is half of connected range of devices, and the initial position of aerial node is the origin of coordinates.

Then, we describe the mechanism of 2D SLMM. For the sake of clarity, we give its trajectory at first (see Figure 6).

The node selects some parameters of mobility before movement, which includes the angular speed, the ending time and the time interval of moving and pausing. Then, the node follows the spreading trajectory of spiral line until the moving time interval elapses, after that it hovers over the current location during the pausing time interval. Once approaches the boundary, the node immediately switches from the current trajectory to the new trajectory which will follow the spiral line of contracting inwardly. Similarly, the node will spread again when it approaches the center of trajectory of spiral line. Finally, the node will repeat the entire process until the ending time has been finished.

B. THE ANNULAR BOUNDARY MODEL

In 2D SLMM, we extend the concept of buffer to circular zone to develop ABM. Compared with rectangular boundary model, ABM can reflect the real situation beside boundaries of region. Obviously, the ABM could effectively limit the trajectory of 2D SLMM into circular buffer (see Figure 7). In contrast, the aerial node will reach boundary without ABM, thereby might suffer the effect of boundary (see Figure 6)

Importantly, some key properties of 2D SLMM have been studied in our previous works (e.g. mathematical results, key

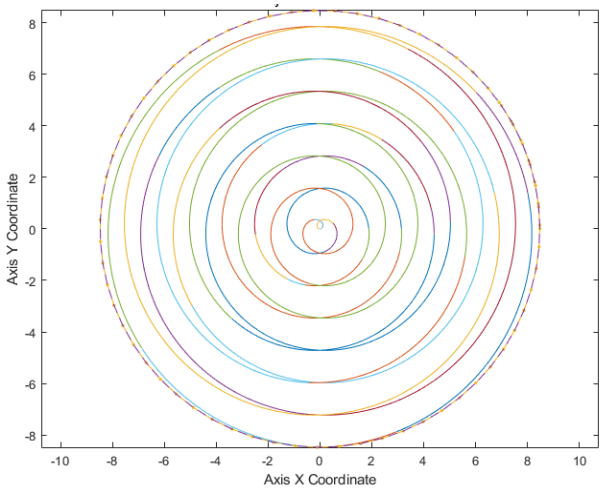

FIGURE 6. The trajectory of 2D SLMM.

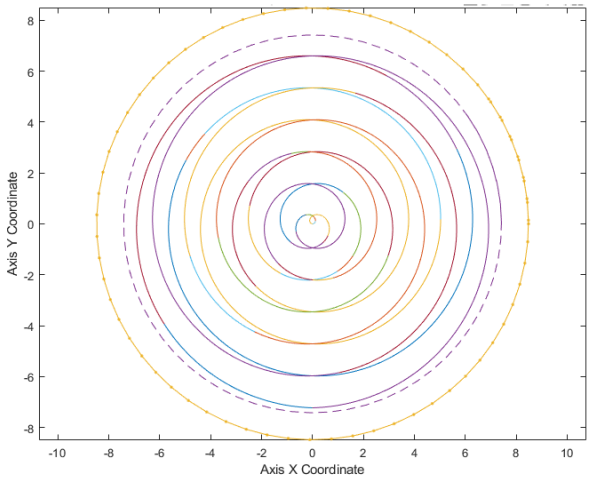

FIGURE 7. The trajectory of 2D SLMM with ABM.

mobility features and network performance). For the sake of space, more details can be found in [29].

Next, we will develop authentic 3D SLMM based on 2D SLMM, such as Z-Or-SLMM and Z-Non-SLMM.

IV. THE AUTHENTIC 3D SLMM

In this section, we will develop authentic 3D SLMM, such as Z-Or-SLMM and Z-Non-SLMM. Firstly, we elaborate mechanism of Z-Or-SLMM and Z-Non-SLMM, respectively. Then, we propose a novel flexible boundary model (FBM) according to the concept of flexible constraint. Finally, we validate the trajectory of 3D SLMM though the real traces.

A. THE MECHANISM OF 3D SLMM

According to the different features, the authentic 3D SLMM could be classified as Z-Or-SLMM and Z-Non-SLMM. Then, we introduce their mechanisms respectively.

1) THE Z-Or-SLMM

In the Z-Or-SLMM, the movement of aerial node mainly includes two aspects. An aspect is horizontal movement in XOY plane, and another aspect is the vertical elevation in Z direction. Certainly, the horizontal movement is independent and orthogonal with the vertical. This situation is suitable for most aerial flight (e.g. aviation or aerial transportation [26]).

Similarly, we give some mobility hypothesis in the Z-Or-SLMM. For the XOY plane, we suppose that the angular speed and the pausing time interval is the uniform distribution, which is similar with 2D SLMM. Moreover, the moving time interval is the exponential distribution with certain coefficient. In addition, the initial position of the aerial node is the origin. For the Z direction, we assume that the altitude of node elevate at a constant speed, and the maximum hovering altitude and the thread pitch has been selected before.

Under the above assumptions, we introduce the mechanism of Z-Or-SLMM. For the sake of clarity, we give its synthetic trajectory before (see Figure 8).

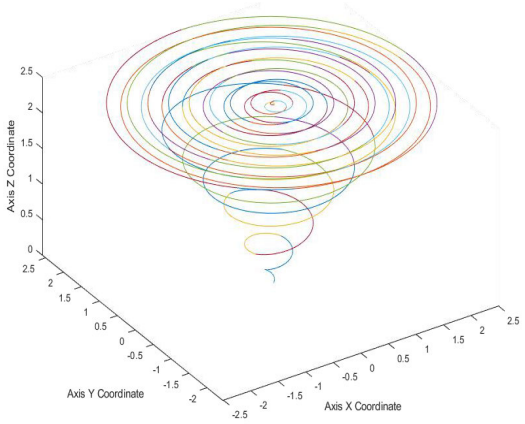

FIGURE 8. The synthetic trajectory of Z-Or-SLMM.

At the beginning, the node selects some key mobility parameters before movement (e.g. angular and vertical speed, hovering altitude, moving and pausing time interval). Then, the node move in the XOY plane until the moving time interval elapses, according to the spreading trajectory of spiral line. After that, it will hover over the current location during the pausing time interval. Meanwhile, the aerial node increase altitude in Z direction at a constant speed, until it reaches hovering altitude. After that, the node will keep at hovering altitude whatever move or hover.

Once boundary approaches, the node switches from the current trajectory to the contracting trajectory of spiral line. Similarly, the node will spread again, as long as it approaches the center of trajectory of spiral line. After each cycle, the node will update many mobility parameters. Finally, the node repeat entire process, until the ending time has been finished.

2) THE Z-NON-SLMM

In Z-Non-SLMM, the horizontal movement is dependent and non-orthogonal with the vertical. In fact, this situation just occurs in some special aviation (e.g. military flight or air show [13]).

Similarly, we give some mobility assumptions in Z-Non-SLMM. Firstly, we suppose that the horizontal and vertical angular speed is the uniform distribution. Then, the moving time interval is the exponential distribution with certain coefficient. Besides, the pausing time interval is the uniform distribution. In addition, the initial position of aerial node is the origin.

For sake of clarity, we give a schematic diagram to elaborate the mechanism of Z-Non-SLMM (See Figure 9,10).

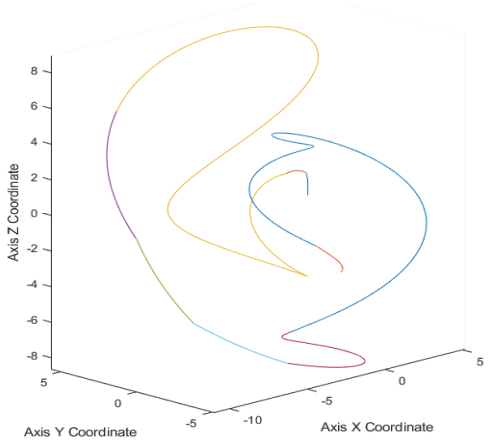

FIGURE 9. The synthetic trajectory of Z-Non-SLMM.

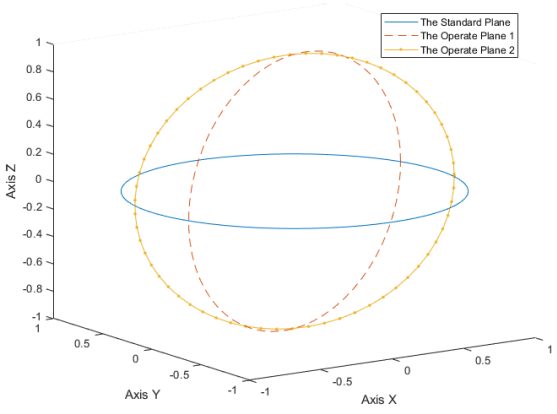

FIGURE 10. The schematic diagram of Z-Non-SLMM.

Firstly, the node selects some mobility parameters before movement (e.g. the horizontal and vertical angular speed, moving and pausing time interval). According to these parameters, the current operating plane can be determined based on standard plane. Then, the node move in the current operating plane until the moving time interval elapses, according to the spreading trajectory of spiral line. After that, it hovers over current location during the pausing time interval.

Once boundary approaches, the node switches from the current trajectory to the contracting trajectory of spiral line. Similarly, the node will spread again, so long as it approaches the center of trajectory of spiral line. After each cycle, some mobility parameters will be updated, and the new operating plane will be determined again. Finally, the node repeat entire process, until the ending time has been finished.

B. THE NOVEL FLEXIBLE BOUNDARY MODEL

In recent years, the idea of flexibility has been introduced into many new products (e.g. flexible material [45] and flexible printed circuits [46]). In simple terms, flexibility means that the object can self-adaptively adjust internal property, according to external change. With some new symbols (See Table 1), we abstract the idea of flexibility in mathematical form below.

$$\begin{aligned} w &= f(x) \\ y &= S + f(w \times C) \end{aligned} \tag{1}$$

TABLE 1. The new symbols in flexibility.

Symbol	Quantity
x	Effect variable
y	Object variable
w	Flexible coefficient
C	Bound variable
S	Constant variable
$f(\bullet)$	A relationship of function

Obviously, the object variable in equation (1) can self adaptively vary though the effect of flexible coefficient with the change of effect variable.

Then, we propose a novel boundary model (i.e. FBM) based on the idea of flexibility. Specially, we consider flexible constraint of 3D take-off path to minimize departure time.

According to equation (1), the effect variable is the distance of deviating central axis, which reflects the relationship between the node and boundary. Besides, the object variable is real time location of aerial node, which embodies authentic situation of aerial flight. In addition, the bound variable is the thread pitch of trajectory of spiral line. And the constant variable is minimum buffer distance, which ensures necessary safety of aerial node.

Next, we introduce FBM into Z-Or-SLMM to investigate the actual effect of flexible constraint (See Figure 11,12).

Clearly, the spacing distance in normal departure path is uniform, and its span can gradually increase to range (See Figure 11). It is because the thread pitch of spiral line is always constant in the Z-Or-SLMM, thereby the distance between the node and central axis could gradually add.

In contrast, the spacing distance gradually decreases in the departure path with FBM, and its span can be greatly limited by FBM to the range (See Figure 12). That is because

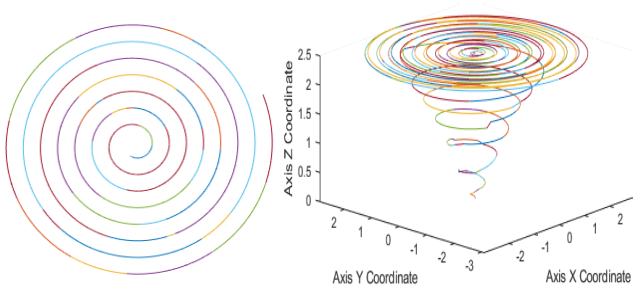

FIGURE 11. The normal departure path.

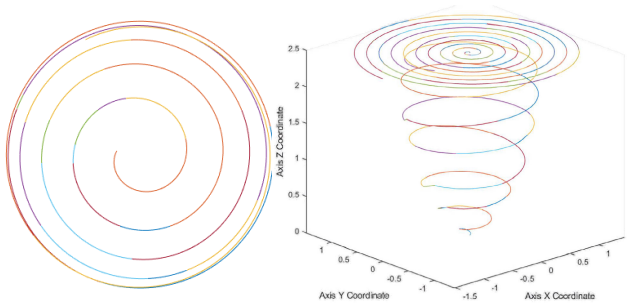

FIGURE 12. The departure path with FBM.

the thread pitch of spiral line can be affected by flexible coefficient, so that its thread pitch can decrease with the increase of relative distance.

Compared with the normal, the 3D departure path is shorter under FBM. It means that real time location of nodes can be greatly confined to a limited 3D space, so that an expected departure time can be obtained by selecting appropriate flexible factor. Hence, FBM is very suitable to cope with some special situations in SAR (e.g. emergency takeoff or quite limited scene).

C. THE VALIDATION OF TRAJECTORY OF 3D SLMM

In the [29], we have extracted some important mobility parameters from the real traces collected in actual scene (e.g. angular speed, moving and pausing time interval) (See Figure 13).

Here, we directly introduce these extracted mobility parameters into 3D SLMM to validate the authenticity of synthetic trajectory (See Figure 14, 15).

Clearly, the traces-based trajectory is almost similar to the synthetic trajectory whatever under Z-Or-SLMM or Z-Non-SLMM. It means that 3D SLMM can accurately imitate true aerial mobility features in the actual scene. Hence, 3D SLMM is suitable and credible for SAR.

Next, we will discuss some key mathematical features of 3D SLMM, such as the mathematical expression, and the 3D distribution of spatial node at steady status.

V. THE MATHEMATICAL FEATURE OF 3D SLMM

In this section, we will discuss some key mathematical feature of 3D SLMM. Firstly, we abstract the specific mathematical

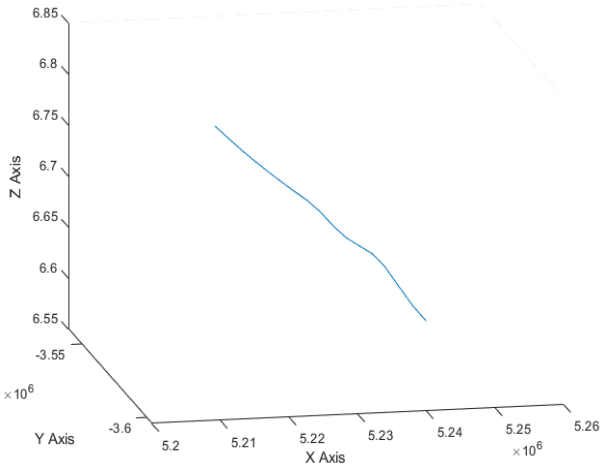

FIGURE 13. The real traces of flight with ENU coordinate.

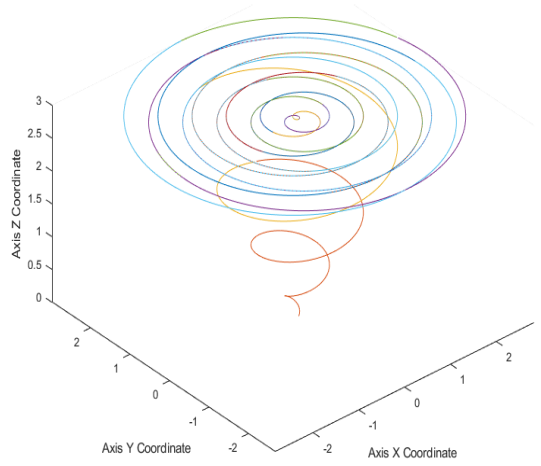

FIGURE 14. The traces-based trajectory of Z-Or-SLMM.

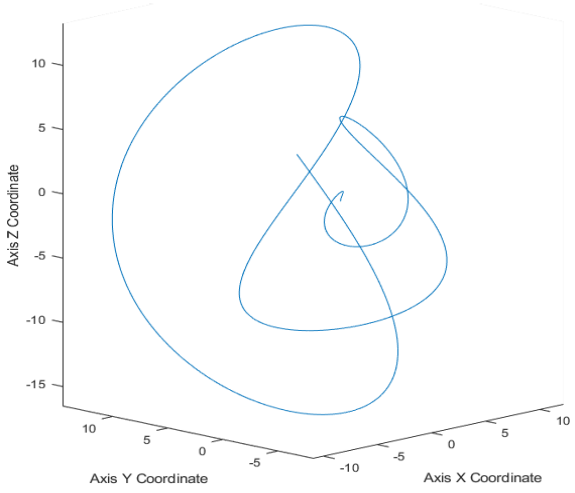

FIGURE 15. The traces-based trajectory of Z-Non-SLMM.

expression of 3D SLMM. Then, some key properties of 3D SLMM are given in the form of theorem. Finally, we propose a novel method of front and top view (FTV) to validate the 3D distribution of spatial node of 3D SLMM.

A. THE MATHEMATICAL EXPRESSION OF 3D SLMM

Here, we abstract specific mathematical expression of Z-Or-SLMM and Z-Non-SLMM, respectively. For the sake of clarity, we define some new symbols in 3D space (See Table 2).

TABLE 2. The new mobility symbols in 3D space.

Symbol	Quantity
V_z	vertical speed
$Z, Z_{current}$	altitude and current altitude
T_{move}	moving time interval
B_{spiral}	the thread pitch of spiral line
I_{spiral}	the coefficient of spiral line
W_θ, W_φ	angular speed of vertical and horizontal
θ, φ	vertical and horizontal radian
γ	the absolute radian
$\Delta\theta, \Delta\varphi, \Delta Z$	the change of vertical, horizontal and altitude
$\theta_{\text{current}}, \varphi_{\text{current}}$	current angle of vertical and horizontal
D_{start}	the initial distance from the origin
$(X_{\text{start}}, Y_{\text{start}}, Z_{\text{start}})$	the initial coordinate of node
(X, Y, Z)	3D coordinate of node
PDF	probability density function
CDF	cumulative distribution function
FDF	frequency distribution function

1) THE Z-Or-SLMM

According to the mechanism, the horizontal movement is orthogonal and independent with the vertical direction in the Z-Or-SLMM. Hence, the actual movement of nodes can be analyzed in horizontal and vertical aspects, respectively.

For horizontal aspects, the movement of node still keeps the same trajectory of 2D SLMM, and the corresponding expression can be expressed below.

$$\begin{aligned} \Delta\varphi &= W_\varphi \times T_{move} \\ D_{start} &= \sqrt{X_{start}^2 + Y_{start}^2} \end{aligned} \tag{2}$$

If the node follows spreading or contracting trajectory, entire movement will abide by under left or right equations, respectively.

$$\begin{aligned} \varphi &= \varphi_{current} + \Delta\varphi \quad \varphi = \varphi_{current} - \Delta\varphi \\ I_{spiral} &= D_{start} + B_{spiral} \times \varphi \quad I_{spiral} = D_{start} + B_{spiral} \times (-\varphi) \\ X &= I_{spiral} \times \cos(\varphi) \quad X = I_{spiral} \times \cos(-\varphi) \\ Y &= I_{spiral} \times \sin(\varphi) \quad Y = I_{spiral} \times \sin(-\varphi) \end{aligned} \tag{3}$$

For vertical aspects, the node elevates altitude at a constant speed, until it reaches hovering altitude. Hence, the vertical movement follows under formulas.

$$\begin{aligned} \Delta Z &= V_z \times T_{move} \\ Z &= Z_{current} + \Delta Z \end{aligned} \tag{4}$$

Combined both aspects, the real time location of node can be obtained (i.e. (X, Y, Z)).

2) THE Z-Non-SLMM

In the Z-Non-SLMM, the horizontal movement is dependent with the vertical. Hence, we abstract its mathematical expression below.

$$\begin{aligned} \Delta\theta &= W_\theta \times T_{move} \\ \Delta\varphi &= W_\varphi \times T_{move} \\ \theta &= \theta_{\text{current}} + \Delta\theta \\ \varphi &= \varphi_{\text{current}} + \Delta\varphi \\ \gamma &= \sqrt{\theta^2 + \varphi^2} \\ D_{start} &= \sqrt{X_{start}^2 + Y_{start}^2 + Z_{start}^2} \end{aligned} \tag{5}$$

If the node follows the spreading or contracting trajectory of spiral line, the relevant movement will obey under left or right formulas, respectively.

$$\begin{aligned} I_{spiral} &= D_{start} + B_{\text{spiral}} \times \gamma \quad I_{spiral} = D_{start} + B_{\text{spiral}} \times (-\gamma) \\ X &= I_{spiral} \times \sin(\theta) \times \cos(\varphi) \\ X &= I_{spiral} \times \sin(-\theta) \times \cos(-\varphi) \\ Y &= I_{spiral} \times \sin(\theta) \times \cos(\varphi) \\ Y &= I_{spiral} \times \sin(-\theta) \times \cos(-\varphi) \\ Z &= I_{spiral} \times \cos(\theta) \quad Z = I_{spiral} \times \cos(-\theta) \end{aligned} \tag{6}$$

B. THE KEY PROPERTY OF 3D SLMM

Based on specific mathematical expression, we give some key properties of 3D SLMM in form of theorem.

Theorem 1: We assume that the thread pitch B_0 and the maximum polar angle $\varphi_{\max}$ can be kept constant. Then, the PDF of spatial nodes at steady state in the Z-Or-SLMM approximately is the uniform distribution, and can be expressed as below.

$$\begin{aligned} &P_{Z-Or-SLMM} \\ &= \frac{1}{B_0}\left[\varphi_{\max}\sqrt{\varphi_{\max}^2 + 1} + \ln\left(\varphi_{\max} + \sqrt{\varphi_{\max}^2 + 1}\right)\right] \end{aligned} \tag{7}$$

Notes that the proof of theorem 1 is provided in Appendix A.

Theorem 2: We assume that the horizontal and vertical speed of aerial node is independent identically distributed, and the thread pitch B_0 and the maximum polar angle $\varphi_{\max}$ can be kept constant. Then, the PDF of spatial nodes at steady status in the Z-Non-SLMM is approximately the uniform distribution, and can be expressed as below.

$$P_{Z-Non-SLMM} = \frac{1}{B_0\varphi_{\max}}\left[1 + \sqrt{1 + \sin^2(\varphi_{\max})}\right] \tag{8}$$

Notes that the proof of theorem 2 is provided in Appendix B.

Theorem 3: We assume that the ending time of aerial node is sufficient in the Z-Or-SLMM. Then, the FDF of

Z-Or-SLMM can be expressed as below.

$$F_{Z-Or-SLMM}(\varphi) = \frac{\varphi}{B_0}\left[\varphi_{\max}\sqrt{\varphi_{\max}^2+1} + \ln\left(\varphi_{\max} + \sqrt{\varphi_{\max}^2+1}\right)\right] \quad (9)$$

Theorem 4: We assume that the ending time of aerial node is sufficient in the Z-Non-SLMM. Then, the FDF of Z-Non-SLMM can be expressed as below.

$$F_{Z-Non-SLMM}(\varphi) = \frac{\varphi}{B_0\varphi_{\max}}\left[1 + \sqrt{1+\sin^2(\varphi_{\max})}\right] \quad (10)$$

Notes that the proof of theorem 3 and 4 are provided in Appendix C.

C. THE VALIDATION OF DISTRIBUTION OF SPATIAL NODE OF 3D SLMM

Here, we propose a novel method of front and top view (FTV) to investigate 3D distribution of spatial node of 3D SLMM.

1) THE MECHANISM OF FTV

In the FTV, we define the negative direction of axis of x as the front direction (See Figure 16). In other words, the front view is projection of nodes in YOZ plane. Similarly, the negative direction of axis of z is defined as the top direction, thereby the top view is projection of nodes in XOY plane.

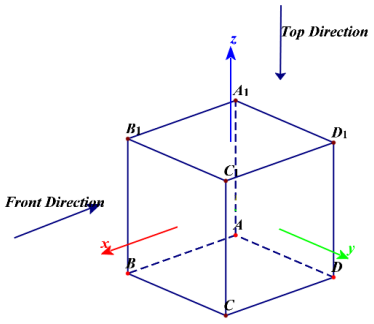

FIGURE 16. The main direction in the FTV.

In this way, we can split 3D PDF of spatial nodes into two 2D PDF to investigate distribution in front view and top view respectively. Then, we can evaluate the approximate 3D distribution of spatial nodes at steady status according to the front and top view.

Certainly, the distribution of spatial nodes is independent with each other in front and top view due to orthogonality. Thus, the 3D approximate distribution of spatial nodes can be restructured by the 2D distribution in front and top view.

2) THE VALIDATION OF 3D PDF

With the FTV, we estimate 3D distribution of spatial nodes at steady status in some 3D mobility models (e.g. 3D-RWP, 3D-GM, 3D-ST and 3D-SLMM) (See Figure 17-22).

In the 3D RWP, most nodes are unevenly distributed in central area whatever in front and top view (See Figure 17), so that the 3D distribution of spatial nodes is not uniform at steady status. That is because any waypoint is randomly selected in 3D space, thereby most destination will be selected in central area with high possibility according to the theory of central limitation (i.e. density wave [50]).

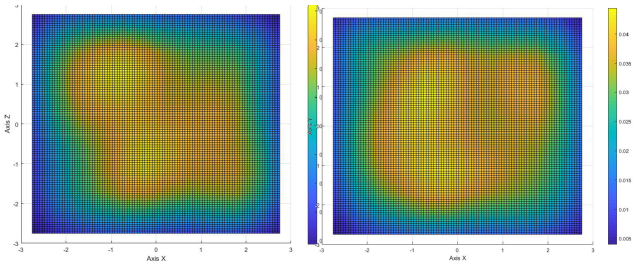

FIGURE 17. The PDF of front and top view of 3D RWP.

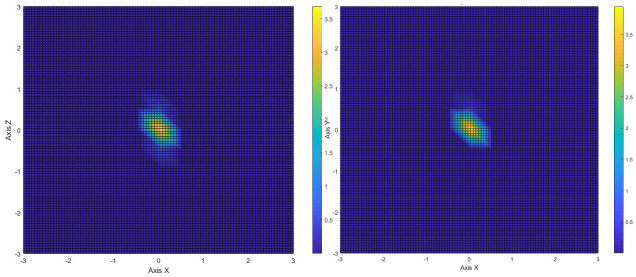

FIGURE 18. The PDF of front and top view of 3D GM.

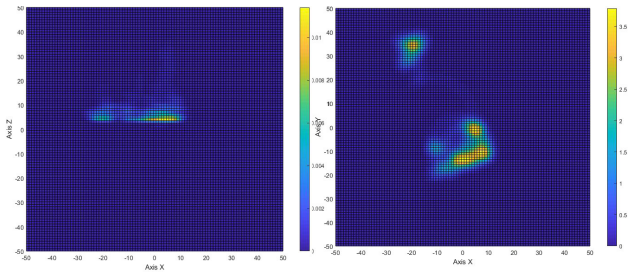

FIGURE 19. The PDF of front and top view of Z-Independent ST.

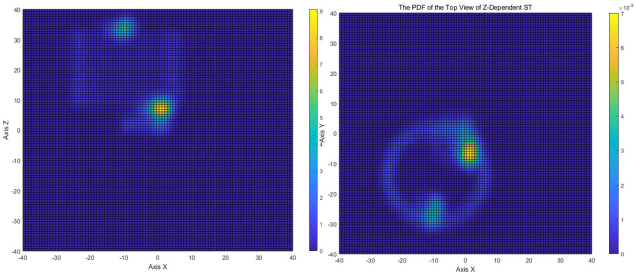

FIGURE 20. The PDF of front and top view of Z-Dependent ST.

Similarly, most nodes are unevenly concentrated within the central area in front and top view under 3D GM (See Figure 18), thus its 3D distribution of spatial nodes is also not uniform at steady status. It is because current speed and direction is always dependent with the previous, thereby adjacent destination of node exists quite higher correlation.

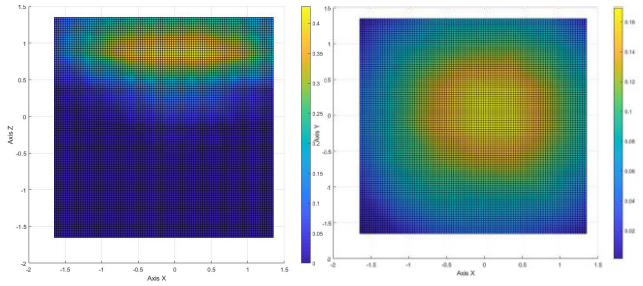

FIGURE 21. The PDF of front and top view of Z-Or-SLMM.

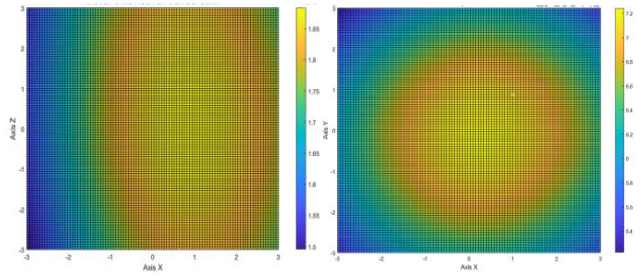

FIGURE 22. The PDF of front and top view of Z-Non-SLMM.

In Z-Independent ST, the node is mainly concentrated within certain horizontal range in front view. In contrast, most nodes are distributed in some hotspots in the top view (See Figure 19). Thus, it is not uniform 3D distribution at steady status. It is because the horizontal movement is always independent with the vertical, thereby most nodes can obtain effective control of altitude. Besides, the adjacent location not deviates much due to smooth turning path.

Under the Z-Dependent ST, most nodes are merely distributed in some hotspots in front and top view (See Figure 20). An eligible reason is the node can freely move in entire 3D space without effective control of altitude. Hence, its 3D PDF is also uneven at steady status.

Ignored minor effect of takeoff, most nodes in Z-Or-SLMM, as theorem 1 say, can be concentrated at hovering altitude in front view. Finally, the node evenly access entire area in top view (See Figure 21). The cause is because the horizontal movement always is orthogonal and independent with the vertical, thereby the horizontal spread greatly maintains the uniform distribution of 2D SLMM. In addition, most nodes can be effectively limited at hovering altitude in Z-Or-SLMM. Hence, the theorem 1 is credible, and its 3D PDF of spatial nodes is uniform at steady status.

In the Z-Non-SLMM, most nodes are distributed within circular area whatever in front and top view (See Figure 22). It is because horizontal movement is not independent with the vertical, so that the node can maintain the uniform distribution of 2D SLMM in both horizontal and vertical aspects. The phenomenon greatly validates theorem 2, that is the PDF of spatial nodes is the uniform distribution in the whole 3D space at steady status.

3) THE VALIDATION OF 3D FDF

In [29], we find that the FPF evaluate 2D distribution of spatial nodes with higher precision, compared with PDF. Here, we introduce FTV into FDF to investigate 3D distribution of spatial nodes of 3D SLMM.

In 3D RWP, we more clearly see that most node still is unevenly distributed in the front and top view (See Figure 23). It is because the destination of node can be randomly selected in whole 3D space.

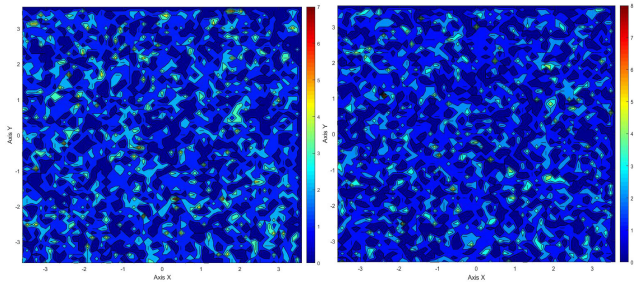

FIGURE 23. The FDF of front and top view of 3D RWP.

In 3D GM, many nodes are mainly distributed within the certain region in front view. Meanwhile, most nodes are concentrated in the top of top view (See Figure 24). The credible reason is the adjacent position of node always deviates minor due to the higher correlation of speed and direction.

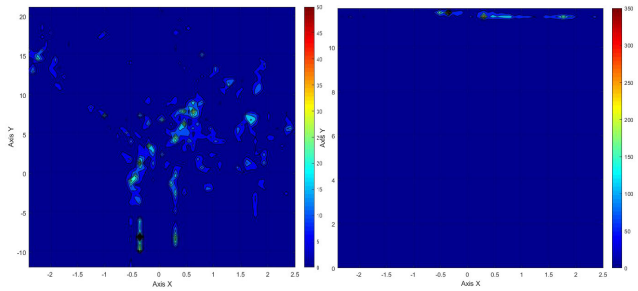

FIGURE 24. The FDF of front and top view of 3D GM.

In Z-Independent ST, most nodes are concentrated in bottom of front view (See Figure 25). It is because the altitude of node can be continuously varied. In contrast, many nodes are distributed in some hotspots regions of top view. It is because the radius of nodes is always randomly selected before movement.

In Z-Dependent ST, most nodes are distributed in some hotspot areas in the front and top view (See Figure 26). An eligible explanation is the altitude and horizontal location of node are able to freely change due to the loss of orthogonality.

In Z-Or-SLMM, most nodes are distributed in the top of front view (See Figure 27). That is because most nodes, as the theorem 3 say, will be mainly concentrated at hovering altitude, compared minor effect of takeoff. Besides, all nodes are distributed in the central region of top view. It is because the node can uniformly visit whole horizontal region, so long as it reaches hovering altitude.

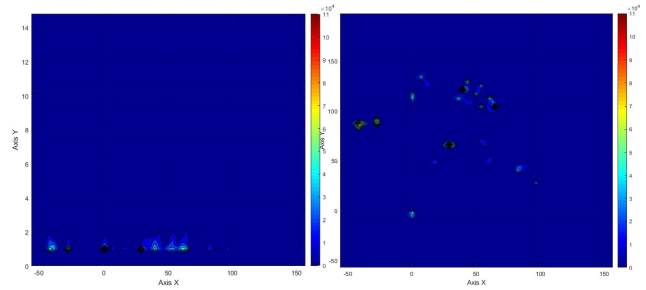

FIGURE 25. The FDF of front and top view of Z-Independent ST.

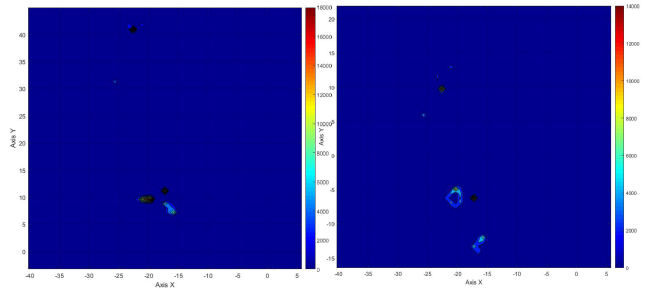

FIGURE 26. The FDF of front and top view of Z-Dependent ST.

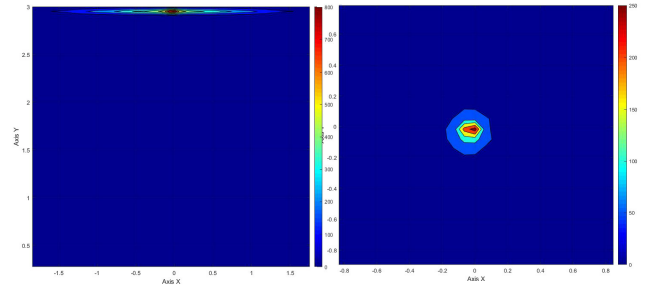

FIGURE 27. The FDF of front and top view of Z-Or-SLMM.

In Z-Non-SLMM, most nodes can be distributed in the central region in front and top view (See Figure 28). Ignored the effect of lack of data, the result greatly verifies the theorem 4 that the node can evenly move in whole 3D space.

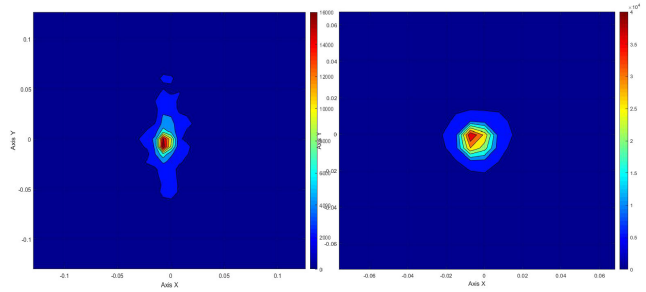

FIGURE 28. The FDF of front and top view of Z-Non-SLMM.

Next, we will investigate some key mobility features of 3D SLMM, such as the smoothness of 3D trajectory and 3D connectivity coverage.

VI. THE MOBILITY FEATURE OF 3D SLMM

In this section, we will investigate some mobility feature of 3D SLMM. Firstly, we mathematically define some key metric of 3D mobility, such as the smoothness of 3D trajectory and 3D connectivity coverage. Then, we evaluate mobility feature of 3D SLMM with these metric.

A. THE 3D MOBILITY METRICS

Here, we mainly focus the smoothness of 3D trajectory and 3D connectivity coverage.

1) THE SMOOTHNESS OF 3D TRAJECTORY

Based on digital signal processing (e.g. [51], [52]), we propose a novel metric (i.e. the degree of smoothness) in [29] to quantitatively evaluate smoothness of 2D trajectory. Here, we extend this metric to 3D space.

Definition 1: We assume that the 3D trajectory can be written as the form of parametric vector.

$$r = (X, Y, Z) = (x(t), y(t), z(t)) \tag{11}$$

Then, the relative vector of first and second order derivative is obtained as below formulas, respectively.

$$\begin{aligned} r' &= (x'(t), y'(t), z'(t)) \\ r'' &= (x''(t), y''(t), z''(t)) \end{aligned} \tag{12}$$

Hence, its curvature can be expressed below.

$$K(t) = \frac{\left|r' \times r''\right|}{|r'|^{\frac{3}{2}}} \tag{13}$$

Thus, the degree of 3D smoothness can be obtained as below.

$$SM(t) = K'(t) \tag{14}$$

Specially, this 3D trajectory is considered as smooth if the next condition is true.

$$\lim_{t\to\infty} SM(t) > 0 \quad \text{or} \quad \lim_{t\to\infty} SM(t) < 0 \tag{15}$$

2) THE 3D CONNECTIVITY COVERAGE

As we know, the connectivity is related to many factors (e.g. sending powers, altitudes, channels, environments and receiver property).

The coverage probability of connectivity has been evaluated in many works, based on signal to interference radio (e.g. [42], [43], [47], [49], [53]). Certainly, it will bring much high complexity when we mainly analyze network property.

Here, we redefine connectivity with second definitions in [48]. In this way, we utilize the valid connected range as the result of considering all influence factors of connectivity. In other words, the pairs of aerial node x, y could connect with each other, if the Euclidean distance $d(x, y)$ between them is less than or equal to the valid connected range R_{com}. That is

$$C(x, y) = \begin{cases} 1, & d(x, y) \le R_{com} \\ 0, & other \end{cases} \tag{16}$$

In which the 1 means valid connectivity, and the 0 means lost connectivity.

According to geometrical relationship, the 3D covered area can be expressed at below (See Figure 29).

$$P(t) = \begin{cases} \pi(R_{com}^2 - h^2), & h > h_{low} \\ 0, & other \end{cases} \tag{17}$$

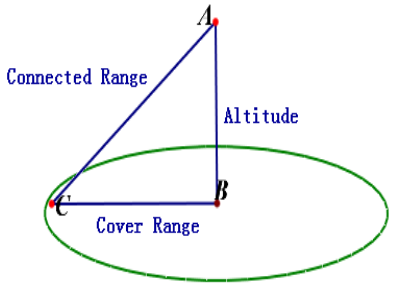

FIGURE 29. The schematic diagram of valid connection.

In which the h means current altitude of aerial node, and h_{low} means the minimum threshold of valid altitude.

Here, we propose two metric to estimate the capacity of connectivity coverage in different aspects (i.e. the ratio of coverage and the convergence time).

Definition 2: We assume that the area of target zone and covered zone could be marked as S and $P(t)$, respectively. Then, we define the ratio of coverage CR as below.

$$CR = \sup(\frac{P(t)}{S}) \tag{18}$$

In addition, we should introduce a new symbol before another definition (i.e. $x = G[y(x)]$). It means that the corresponding variable x when the value of function equal with $y(x)$.

Definition 3: Similarly, we define the convergence time CT as below.

$$CT = \inf G\left[\sup(\frac{P(t)}{S})\right] \tag{19}$$

Clearly, the CR means that the maximum ratio of covered zone in entire zone (See Definition 2). Similarly, the CT means that the corresponding time when aerial node reaches maximum coverage ratio (See Definition 3). Therefore, the reliability and timeliness of connectivity coverage could be estimated.

B. THE EVALUATION OF 3D MOBILITY FEATURE

Next, we evaluate some key mobility features of 3D SLMM though simulation.

Here, we imitate a disaster rescue scene where most architecture has been destroyed by the earthquake. We assume that the potential searching region is 200m∗200m, and the initial location of aerial node is the center of the whole region. Besides, we suppose that the connected range of aerial node is 12m, and the valid threshold of altitude is 5m.

For the mobility of each node, we select some eligible parameters in different model to guarantee that the mobility of each step can be kept almost consistent. For example, we select 5 m/s as maximum running speed in 3D RWP and 3D GM. Besides, we select 5m/s and pi/2 rad/s as the maximum vertical and angular speed in 3D ST and 3D SLMM, respectively. Moreover, the mean and variance of pausing and moving time interval is selected as 1 and 2 in 3D ST and 3D SLMM, respectively. In addition, the hovering altitude is configured as 15m in 3D ST and 3D SLMM. And, the coefficient of correlation is 0.8 in 3D GM.

Then, we execute this simulation at Matlab2019.

1) THE SMOOTHNESS OF 3D TRAJECTORY

We evaluate smoothness of 3D trajectory of different models (e.g. 3D RWP, 3D GM, 3D ST, 3D SLMM).

For the sake of credibility, we perform at least 30 times under each model. Then, we calculate differential coefficient in equation (12), utilizing numerical approximation. Meanwhile, we reduce its data volume by multiplying by certain coefficient and summing subsection. After that, we obtain the optimal result as below.

In 3D RWP, the SM(t) always is almost 0 (See Figure 30). But it does not imply that its 3D trajectory is smooth, and the change of sharp direction not occurs (See Figure 1). A credible reason is that the any path between adjacent waypoint is always straight line which the curvature is zero. Similarly, the similar situation occurs in 3D GM (See Figure 31). It is because its 3D trajectory is constituted by the subsection of straight line which the curvature is 0 (See Figure 2). Certainly, 3D RWP and 3D GM can capture macro mobility of aerial node in wide scene (e.g. aviation [26] or aerial cargo [54]).

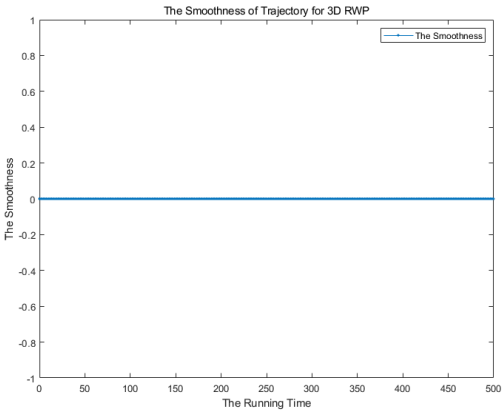

FIGURE 30. The smoothness of trajectory of 3D RWP.

Obviously, the SM(t) occurs 7 and 9 jumping points in Z-Dependent and Z-Independent ST, respectively (See Figure 32, 33). It implies that their 3D trajectory might occur 7 and 9 unsmooth points respectively. That is because the 3D ST still inherit inner defect of 2D ST (See Figure 5), so that some unsmooth points might be produced at adjacent time interval. Thus, the 3D trajectory of 3D ST is not smooth.

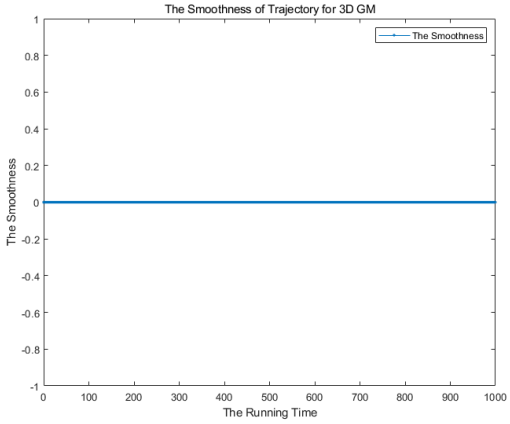

FIGURE 31. The smoothness of trajectory of 3D GM.

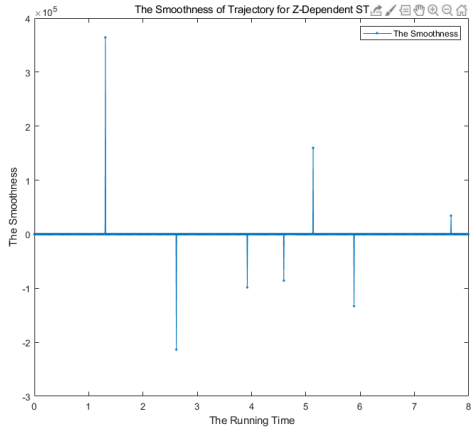

FIGURE 32. The smoothness of trajectory of Z-Dependent ST.

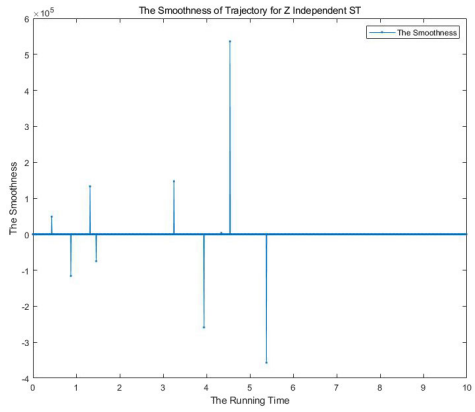

FIGURE 33. The smoothness of trajectory of Z-Independent ST.

In 3D SLMM, the SM(t) all can be kept almost 0 (See Figure 34, 35). It is because the 3D SLMM greatly maintains similar smooth trajectory of 2D ST (i.e. the aerial node always follows smooth trajectory of spiral line) (See Figure 6). Therefore, their 3D trajectory is smooth.

2) THE 3D CONNECTIVITY COVERAGE

We estimate the capacity of 3D connectivity coverage under the typical model providing valid connectivity to

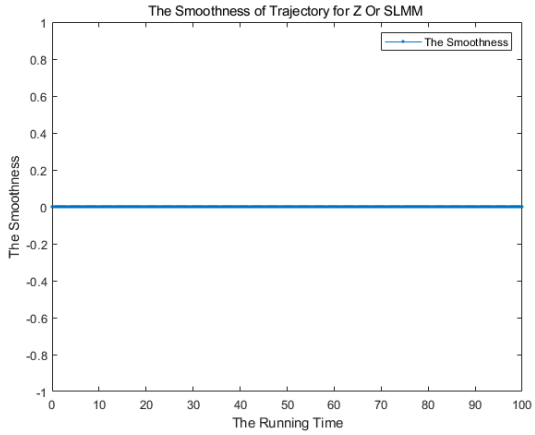

FIGURE 34. The smoothness of trajectory of Z-Or-SLMM.

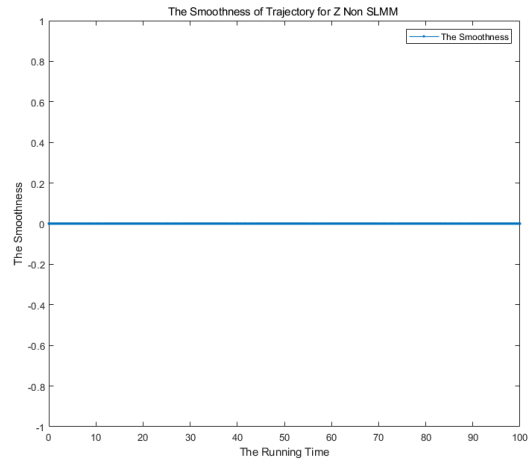

FIGURE 35. The smoothness of trajectory of Z-Non-SLMM.

ground devices (e.g. 3D RWP, 3D GM, Z-Independent ST, Z-Or-SLMM). Other mobility models facing with special flight are not discussed here (e.g. Z-Dependent ST, Z-Non-SLMM).

To reduce complexity, we sample each 3D trajectories with low precision, and calculate the covered area at each sample point. In addition, we reckon the area of entire zone, and obtain their preliminary results. To improve credibility, we complete at least 100 times to calculate their 95% confidence interval. Finally, we obtain optimal results as below.

At aspects of CR, the CR reaches almost 87% in 3D RWP (See Figure 36). That is because the aerial node can provide valid connectivity to the device on the ground, so long as its altitude is within effective altitude range. Hence, the CR gradually improves with the increase of number of way points.

In 3D GM, the CR can be kept almost 0. A reasonable cause is the aerial node cannot exceed the threshold of valid altitude in limited time due to the high correlation of speed and direction.

In Z-independent ST, the CR is approximate 68%. It is because the aerial node will randomly move in entire

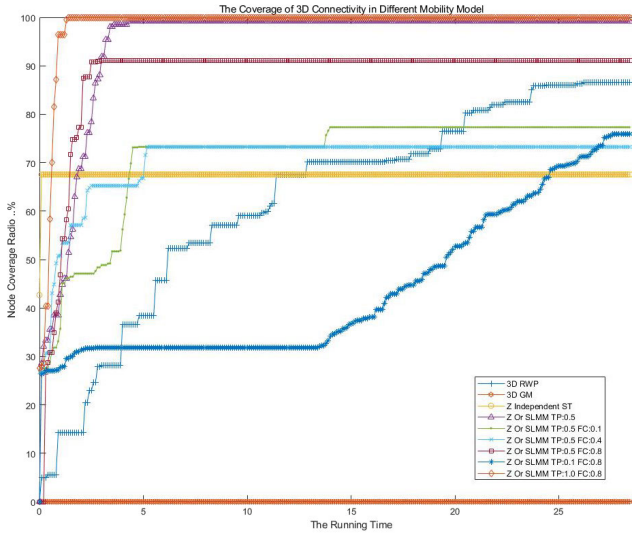

FIGURE 36. The coverage of 3D connectivity under different models.

3D space without effective altitude control, thereby the aerial node cannot provide connectivity once its altitude reaches the effective altitude range. Thus, its covered area is quite limited.

In contrast, the CR can approach 100% whatever under Z-Or-SLMM which the thread pitch (TP) is 0.5m or under Z-Or-SLMM which TP and the flexible factors (FC) is 0.5m and 1.0m. Under Z-Or-SLMM of same TP, the CR is decreased to 72% when FC is 0.1. That is because the 3D trajectory can be effectively limited by FBM at departure stage, so that a little benefit of coverage may be lost.

However, the CR can improve gradually with the increase of FC. For example, the CR is almost 72% when FC is 0.1, but the CR could approach 92% when FC is 0.8. The eligible explanation is that 3D trajectory can be gradually recovered when the flexible constraint is relaxed, thereby the loss of CR can be reduced.

Moreover, the change of TP will influence the CR when FC is same. As a typical contrast, the CR is almost 74% when TP is 0.1m, but the CR rapidly approaches 100% when the TP is 1m. It is because the TP change spacing distance of trajectory, which will influence the covered area on the ground. Hence, the CR will gradually reduce with the decrease of TP.

For the aspect of CT, the CT lasted more than 28 minutes in 3D RWP. This is because it's the aerial node may exceed effective altitude range with high probability because of random location, thereby cannot provide valid connectivity to the device on the ground.

Obviously, the CT is quite large in 3D GM. It is because the aerial node may cost more time to reach certain altitude threshold, due to the high correlation of adjacent location. In Z-Independent ST, the CT is less than 1 minute. It is because the aerial node can rapidly reach steady status, with utilizing random radius and continuous altitude.

In Z-Or-SLMM, the CT approach 1.5 minutes when TP and FC are 1.0m and 0.8 respectively. It is because the aerial node can provide valid connectivity, as long as its altitude beyond certain valid threshold. Thus, most target has been covered by aerial node at the departure stage.

Under Z-Or-SLMM of same FC, the change of TP largely influences the CT. For example, the CT is almost 27 minutes when TP is 0.1m, and the CT is almost 2.8 minutes when the TP is 0.5m. In other words, the CT will gradually decrease with the increase of TP. An eligible reason is that the TP determines the spacing distance of spiral line, thereby the aerial node can rapidly access the whole region when the TP is large.

Compared with the situation without FC, the CT is improved to 13.5 minutes when TP is 0.5 and FC is 0.1. The possible reason is that the FC greatly limits the 3D trajectory at departure stage, thereby the benefit of relevant coverage may be lost.

Besides, the CT gradually reduces with the increase of FC when TP is same. For example, the CT is almost 14.5 minutes when FC is 0.1, but the CT approach 5.5 minutes when FC is 0.4, and the CT is almost 3.6 minutes when FC is 0.8. That is because the benefit of related coverage has been regained with the decrease of FC, so that the CT will be gradually reduced.

VII. CONCLUSION AND FUTURE WORKS

In this paper, we propose authentic 3D SLMM for ABN. Firstly, we review the basic concept of 2D SLMM. Then, we propose authentic 3D SLMM based on 2D SLMM, such as Z-Or-SLMM and Z-Non-SLMM. Meanwhile, we propose a novel flexible boundary model (FBM). The result shows that the FBM can effectively limit 3D trajectory of Z-Or-SLMM at the departure stage. In addition, we validate synthetic trajectory of 3D SLMM through the real traces. Then, we investigate some mathematical features of 3D SLMM (e.g. mathematical expression, the distribution of spatial nodes). Furthermore, we propose a novel method of front and top view to validate mathematical property of 3D SLMM. The simulation shows that Z-Or-SLMM and Z-Non-SLMM all possess uniform distribution of spatial node at steady status. In the further, we define some new metric to evaluate 3D mobility features of 3D SLMM. The result proves that Z-Or-SLMM and Z-Non-SLMM all have smooth 3D trajectory. Compared with other 3D models, the aerial node can rapidly cover the whole target region under the Z-Or-SLMM. Moreover, the flexible constraint can affect 3D coverage efficiency. In other words, appropriate flexible constraint is beneficial, but too much flexible constraint will severely influence the 3D coverage efficiency in turn.

In the future, we hope to evaluate network performance under 3D SLMM by other network simulator although NS2 may not support 3D network. Besides, we will investigate how the FBM affect network property in ABN. Finally, the dynamic connectivity issue should be studied under 3D SLMM.

APPENDIX A

Proof: To prove the theorem 1, we provide some assumptions before. Firstly, we assume that some parameters can be kept constant during entire flight (e.g. hovering altitude h_{hover}, thread pitch B_0, vertical velocity V_z). Besides, we assume that the mean of angular velocity could be indicated as w_0 to simplify this proof. In addition, the time of each cycle and the maximum outspreading radian are expressed as T_{Cycle}, $\varphi_{\max}$, respectively. Due to the symmetry relationship, the outspreading and contracting time approximate with a half of T_{Cycle}.

$$\varphi_{\max} = \sum_{0}^{\frac{T_{cycle}}{2}} \Delta\varphi \tag{20}$$

Next, we start to prove the theorem 1. Here, the curvilinear equation of the Z-Or-SLMM can be expressed as below.

$$\begin{cases} X(t) = B_0 \cos(w_0 t) \\ Y(t) = B_0 \sin(w_0 t) \\ Z(t) = V_z t \end{cases} \tag{21}$$

in which the t express the current running time of the node.

According to the definition, the PDF of Z-Or-SLMM can be showed as below.

$$P_{Z-Or-SLMM} = \frac{1}{L_{spiral}} \tag{22}$$

in which the L_{sprial} express the arc length of whole trajectory of Z-Or-SLMM.

Then, we begin to calculate L_{sprial}. Clearly, the whole process of flight consists of the departure stage and the hovering stage. Due to mutual independence, we can analyze each stage respectively. That is

$$L_{spiral} = L_{departure} + L_{hover} \tag{23}$$

Obviously, the node will move according to the SLMM approaching the hovering altitude. Hence, we utilize directly the previous result of the SLMM to express the arc length at the hovering stage.

$$L_{hover} = B_0 \left[\varphi_{\max} \sqrt{\varphi_{\max}^2 + 1} + \ln\left(\varphi_{\max} + \sqrt{\varphi_{\max}^2 + 1} \right) \right] \tag{24}$$

In the further, we will reckon $L_{departure}$. Clearly, the time reaching the hovering altitude can be expressed at below.

$$t_{hover} = \frac{h_{hover}}{V_z} \tag{25}$$

Next, we express this curvilinear equation of Z-Or-SLMM as the form of vector.

$$\begin{aligned} r(t) &= (X(t), Y(t), Z(t)) \\ &= (B_0 \cos(w_0 t), B_0 \sin(w_0 t), V_z t) \end{aligned} \tag{26}$$

And its first derivative can be showed at below.

$$r'(t) = (-B_0 w_0 \sin(w_0 t), B_0 w_0 \cos(w_0 t), V_z) \tag{27}$$

Then, the module value of its first derivative is shown at below.

$$\begin{aligned} \left| r'(t) \right| &= \sqrt{(X'(t))^2 + (Y'(t))^2 + (Z'(t))^2} \\ &= \sqrt{(-B_0 w_0 \sin(w_0 t))^2 + (B_0 w_0 \cos(w_0 t))^2 + V_z^2} \\ &= \sqrt{(B_0 w_0)^2 + V_z^2} \end{aligned} \tag{28}$$

Therefore, the whole arc length at the departure stage can be reckoned at below.

$$\begin{aligned} &L_{departure} \\ &= \int_0^{t_{hover}} \left| r'(t) \right| dt \\ &= \int_0^{t_{hover}} \sqrt{(B_0 w_0)^2 + V_z^2} dt = \sqrt{(B_0 w_0)^2 + V_z^2} \cdot t \Big|_0^{t_{hover}} \\ &= t_{hover} \sqrt{(B_0 w_0)^2 + V_z^2} = \frac{h_{hover}}{V_z} \sqrt{(B_0 w_0)^2 + V_z^2} \end{aligned} \tag{29}$$

Certainly, the arc length at the departure stage is minor compared with the hovering stage. Here, we ignore the quite limited effect of the departure stage to further simplify the result. So the arc length of entire flight can be expressed at below.

$$\begin{aligned} L_{sprial} &= L_{departure} + L_{hover} \\ &= B_0 \left[\varphi_{\max} \sqrt{\varphi_{\max}^2 + 1} + \ln\left(\varphi_{\max} + \sqrt{\varphi_{\max}^2 + 1} \right) \right] \\ &\quad + \frac{h_{hover}}{V_z} \sqrt{(B_0 w_0)^2 + V_z^2} \\ &\approx B_0 \left[\varphi_{\max} \sqrt{\varphi_{\max}^2 + 1} + \ln\left(\varphi_{\max} + \sqrt{\varphi_{\max}^2 + 1} \right) \right] \end{aligned} \tag{30}$$

Combined the equation (22) and (30), the PDF of Z-Or-SLMM can be calculated.

$$\begin{aligned} &P_{Z-Or-SLMM} \\ &= \frac{1}{L_{spiral}} \\ &= \frac{1}{B_0 \left[\varphi_{\max} \sqrt{\varphi_{\max}^2 + 1} + \ln\left(\varphi_{\max} + \sqrt{\varphi_{\max}^2 + 1} \right) \right]} \\ &= \frac{1}{B_0} \left[\varphi_{\max} \sqrt{\varphi_{\max}^2 + 1} + \ln\left(\varphi_{\max} + \sqrt{\varphi_{\max}^2 + 1} \right) \right] \end{aligned} \tag{31}$$

At this point, the proof has been completed.

APPENDIX B

Proof: To prove theorem 2, we should propose some useful assumptions at before. Firstly, we assume that the horizontal and vertical velocity are independent identically distributed, thereby their mean value marked as w_0, w_1 can be used to simplify this proof (i.e. $w_0 \approx w_1$). In addition, the thread pitch B_0 can be kept constant and the preset flight time t_0 have been selected. Besides, the time of each cycle and the

maximum outspreading radian can be marked as T_{cycle}, $\varphi_{\max}$, respectively. Similarly, the under relationship remain valid.

$$\varphi_{\max} = \sum_{0}^{\frac{T_{cycle}}{2}} w_0 \Delta t \tag{32}$$

Next, we begin to prove theorem 2. Here, the curvilinear equation of the Z-Non-SLMM can be expressed as below.

$$\begin{cases} X(t) = B_0 \sin(w_0 t)\cos(w_1 t) \\ Y(t) = B_0 \sin(w_0 t)\sin(w_1 t) \\ Z(t) = B_0 \cos(w_0 t) \end{cases} \tag{33}$$

in which the t express the current running time of the node.

According to the definition, the PDF of the Z-Non-SLMM can be expressed at below.

$$P_{Z-Non-SLMM} = \frac{1}{L_{spiral}} \tag{34}$$

Then, we will mainly reckon L_{spiral}. Similarly, we express this curvilinear equation of Z-Non-SLMM as the form of vector.

$$\begin{aligned} & r(t) \\ &= (X(t), Y(t), Z(t)) \\ &= (B_0 \sin(w_0 t)\cos(w_1 t), B_0 \sin(w_0 t)\sin(w_1 t), B_0 \cos(w_0 t)) \end{aligned} \tag{35}$$

And its first derivative can be showed at below.

$$r'(t) = (X'(t), Y'(t), Z'(t)) \tag{36}$$

Therein,

$$\begin{cases} X'(t) = B_0 \left[w_0 \cos(w_0 t)\cos(w_1 t) - w_1 \sin(w_0 t)\sin(w_1 t)\right] \\ Y'(t) = B_0 \left[w_0 \cos(w_0 t)\sin(w_1 t) + w_1 \sin(w_0 t)\cos(w_1 t)\right] \\ Z'(t) = -B_0 w_0 \sin(w_0 t) \end{cases}$$

In the further, the square of its first derivative can be expressed as below.

$$\begin{aligned} & (X'(t))^2 \\ &= B_0^2 \begin{bmatrix} w_0^2 \cos^2(w_0 t)\cos^2(w_1 t) \\ -2w_0 w_1 \sin(w_0 t)\cos(w_0 t)\sin(w_1 t)\cos(w_1 t) \\ +w_1^2 \sin^2(w_0 t)\sin^2(w_1 t) \end{bmatrix} \\ & (Y'(t))^2 \\ &= B_0^2 \begin{bmatrix} w_0^2 \cos^2(w_0 t)\sin^2(w_1 t) \\ +2w_0 w_1 \sin(w_0 t)\cos(w_0 t)\sin(w_1 t)\cos(w_1 t) \\ +w_1^2 \sin^2(w_0 t)\cos^2(w_1 t) \end{bmatrix} \\ & (Z'(t))^2 \\ &= B_0^2 w_0^2 \sin^2(w_0 t) \end{aligned} \tag{37}$$

And, the module value of the square of its first derivative can be showed as below.

$$\begin{aligned} \left|r'(t)\right| &= \sqrt{(X'(t))^2 + (Y'(t))^2 + (Z'(t))^2} \\ &= \sqrt{B_0^2\left[w_0^2\cos^2(w_0 t) + w_1^2 \sin^2(w_0 t) + w_0^2 \sin^2(w_0 t)\right]} \\ &= B_0\sqrt{w_0^2 + w_1^2 \sin^2(w_0 t)} \end{aligned} \tag{38}$$

Hence, the arc length of the Z-Non-SLMM can be reckoned at below.

$$\begin{aligned} & L_{spiral} \\ &= \int_0^{t_0} \left|r'(t)\right| dt \\ &= B_0 \int_0^{t_0} \sqrt{w_0^2 + w_1^2 \sin^2(w_0 t)} dt \\ &\overset{x=w_0 t}{=} B_0 \int_0^{w_0 t_0} \sqrt{1 + \frac{w_1^2}{w_0^2} \sin^2(x)} dx \\ &\overset{\frac{w_1}{w_0}\approx 1}{=} B_0 \int_0^{w_0 t_0} \sqrt{1 + \sin^2(x)} dx \\ &= B_0 \left[x\sqrt{1+\sin^2(x)}\Big|_0^{w_0 t_0} \right. \\ &\quad \left. - \int_0^{w_0 t_0} x \cdot d\left(\sqrt{1+\sin^2(x)}\right) \right] \\ &= B_0 \left[w_0 t_0 \sqrt{1+\sin^2(w_0 t_0)} \right. \\ &\quad \left. - \int_0^{w_0 t_0} x \cdot \frac{\sin x \cos x}{\sqrt{1+\sin^2(x)}} dx \right] \\ &= B_0 \left[w_0 t_0 \sqrt{1+\sin^2(w_0 t_0)} \right. \\ &\quad \left. - \frac{w_0 t_0}{2} \int_0^{w_0 t_0} \frac{\sin x}{\sqrt{1+\sin^2(x)}} d(\sin x) \right] \\ &\overset{y=\sin x}{=} B_0 \left[w_0 t_0 \sqrt{1+\sin^2(w_0 t_0)} \right. \\ &\quad \left. - \frac{w_0 t_0}{2} \int_0^{\sin(w_0 t_0)} \frac{y}{\sqrt{1+y^2}} dy \right] \\ &= B_0 \left[w_0 t_0 \sqrt{1+\sin^2(w_0 t_0)} \right. \\ &\quad \left. - \frac{w_0 t_0}{4} \int_0^{\sin(w_0 t_0)} \frac{1}{\sqrt{1+y^2}} d(1+y^2) \right] \\ &\overset{z=1+y^2}{=} B_0 \left[w_0 t_0 \sqrt{1+\sin^2(w_0 t_0)} \right. \\ &\quad \left. - \frac{w_0 t_0}{4} \cdot 2z^{\frac{1}{2}}\Big|_1^{1+\sin^2(w_0 t_0)} \right] \\ &= B_0 \left[w_0 t_0 \sqrt{1+\sin^2(w_0 t_0)} \right. \\ &\quad \left. - \frac{w_0 t_0}{2}\left(\sqrt{1+\sin^2(w_0 t_0)} - 1\right) \right] \\ &= B_0 \cdot \frac{w_0 t_0}{2}\left[1 + \sqrt{1+\sin^2(w_0 t_0)}\right] \end{aligned} \tag{39}$$

Due to the relationship of symmetry, the arc length of each cycle of the Z-Non-SLMM can be found as below.

$$\begin{aligned}&\lim_{t_0 \to T_{cycle}} L_{spiral} \\ &= 2B_0 \cdot \frac{\varphi_{\max}}{2}\left[1+\sqrt{1+\sin^2(\varphi_{\max})}\right] \\ &= B_0\varphi_{\max}\left[1+\sqrt{1+\sin^2(\varphi_{\max})}\right] \end{aligned} \tag{40}$$

Combined with the equation (34) and (40), the PDF of the Z-Non-SLMM is expressed at below.

$$\begin{aligned}P_{Z-Non-SLMM} &= \frac{1}{L_{spiral}} \\ &= \frac{1}{B_0\varphi_{\max}\left[1+\sqrt{1+\sin^2(\varphi_{\max})}\right]} \\ &= \frac{1}{B_0\varphi_{\max}}\left[1+\sqrt{1+\sin^2(\varphi_{\max})}\right] \end{aligned} \tag{41}$$

At this point, this proof has been completed.

APPENDIX C

Proof: To prove the theorem 3 and 4, we assume that the ending time is sufficient. In this case, the FDF could approximate with the CDF. That is

$$F(\varphi) \approx \lim_{t\to\infty} C(\varphi) \tag{42}$$

For the Z-Or-SLMM, its CDF can be expressed as below.

$$\begin{aligned}&C_{Z-Or-SLMM}(\varphi) \\ &= P(\varphi' < \varphi) \\ &= \int_{-\infty}^{\varphi} P_{Z-Or-SLMM}(\varphi')d\varphi' \\ &= \int_{-\infty}^{\varphi} \frac{1}{B_0}\left[\varphi_{\max}\sqrt{\varphi_{\max}^2+1}\right. \\ &\quad \left.+\ln\left(\varphi_{\max}+\sqrt{\varphi_{\max}^2+1}\right)\right]d\varphi' \\ &= \frac{\varphi}{B_0}\left[\varphi_{\max}\sqrt{\varphi_{\max}^2+1}+\ln\left(\varphi_{\max}+\sqrt{\varphi_{\max}^2+1}\right)\right] \end{aligned} \tag{43}$$

Therefore, the FDF of Z-Or-SLMM can be reckoned at below.

$$\begin{aligned}&F_{Z-Or-SLMM}(\varphi) \\ &\approx \lim_{t\to\infty} C_{Z-Or-SLMM}(\varphi) \\ &= \frac{\varphi}{B_0}\left[\varphi_{\max}\sqrt{\varphi_{\max}^2+1}+\ln\left(\varphi_{\max}+\sqrt{\varphi_{\max}^2+1}\right)\right] \end{aligned} \tag{44}$$

Similarly, the CDF of Z-Non-SLMM can be expressed as below.

$$\begin{aligned}&C_{Z-Non-SLMM}(\varphi) \\ &= P(\varphi' < \varphi) \\ &= \int_{-\infty}^{\varphi} P_{Z-Non-SLMM}(\varphi')d\varphi' \\ &= \int_{-\infty}^{\varphi} \frac{1}{B_0\varphi_{\max}}\left[1+\sqrt{1+\sin^2(\varphi_{\max})}\right]d\varphi' \\ &= \frac{\varphi}{B_0\varphi_{\max}}\left[1+\sqrt{1+\sin^2(\varphi_{\max})}\right] \end{aligned} \tag{45}$$

Hence, the FDF of Z-Non-SLMM is shown as below.

$$\begin{aligned}&F_{Z-Non-SLMM}(\varphi) \\ &\approx \lim_{t\to\infty} C_{Z-Non-SLMM}(\varphi) \\ &= \frac{\varphi}{B_0\varphi_{\max}}\left[1+\sqrt{1+\sin^2(\varphi_{\max})}\right] \end{aligned} \tag{46}$$

At this point, this proof has been completed.

REFERENCES

[1] J. Kibilda, A. B. MacKenzie, M. J. Abdel-Rahman, S. K. Yoo, S. L. Cotton, N. Marchetti, W. Saad, W. G. Scanlon, A. Garcia-Rodriguez, L. G. Giordano, D. Lopez-Perez, H. Claussen, and L. A. DaSilva, "Indoor millimeter-wave systems: Design and performance evaluation," *Proc. IEEE*, vol. 108, no. 6, pp. 923–944, Jun. 2020, doi: 10.1109/JPROC.2020.2989189.

[2] A. Zhou, S. Xu, S. Wang, J. Huang, S. Yang, T. Wei, X. Zhang, and H. Ma, "Robotic millimeter-wave wireless networks," *IEEE/ACM Trans. Netw.*, early access, May 19, 2020, doi: 10.1109/TNET.2020.2990498.

[3] B. Wang, R. Zhang, C. Chen, X. Cheng, L. Yang, H. Li, and Y. Jin, "Graph-based file dispatching protocol with D2D-enhanced UAV-NOMA communications in large-scale networks," *IEEE Internet Things J.*, early access, May 15, 2020, doi: 10.1109/JIOT.2020.2994549.

[4] S. Hashima, K. Hatano, E. Takimoto, and E. M. Mohamed, "Neighbor discovery and selection in millimeter wave D2D networks using stochastic MAB," *IEEE Commun. Lett.*, early access, Apr. 30, 2020, doi: 10.1109/LCOMM.2020.2991535.

[5] I. Ioannou, V. Vassiliou, C. Christophorou, and A. Pitsillides, "Distributed artificial intelligence solution for D2D communication in 5G networks," *IEEE Syst. J.*, early access, Apr. 28, 2020, doi: 10.1109/JSYST.2020.2979044.

[6] B. O. Annaidh, P. Fitzgerald, H. Berney, R. Lakshmanan, N. Coburn, S. Geary, and B. Mulvey, "Devices and sensors applicable to 5G system implementations," in *Proc. IEEE MTT-S Int. Microw. Workshop Ser. 5G Hardw. Syst. Technol. (IMWS-5G)*, Dublin, Ireland, Aug. 2018, pp. 1–3.

[7] S. Hayat, E. Yanmaz, and R. Muzaffar, "Survey on unmanned aerial vehicle networks for civil applications: A communications viewpoint," *IEEE Commun. Surveys Tuts.*, vol. 18, no. 4, pp. 2624–2661, 4th Quart., 2016, doi: 10.1109/COMST.2016.2560343.

[8] W. Wang, X. Guan, B. Wang, and Y. Wang, "A novel mobility model based on semi-random circular movement in mobile ad hoc networks," *Inf. Sci.*, vol. 180, no. 3, pp. 399–413, Feb. 2010.

[9] M. Cao, L. Wang, H. Xu, D. Chen, C. Lou, N. Zhang, Y. Zhu, and Z. Qin, "Sec-D2D: A secure and lightweight D2D communication system with multiple sensors," *IEEE Access*, vol. 7, pp. 33759–33770, 2019, doi: 10.1109/ACCESS.2019.2900727.

[10] M. Mozaffari, W. Saad, M. Bennis, Y.-H. Nam, and M. Debbah, "A tutorial on UAVs for wireless networks: Applications, challenges, and open problems," *IEEE Commun. Surveys Tuts.*, vol. 21, no. 3, pp. 2334–2360, 3rd Quart., 2019, doi: 10.1109/COMST.2019.2902862.

[11] Y. Zeng, R. Zhang, and T. J. Lim, "Wireless communications with unmanned aerial vehicles: Opportunities and challenges," *IEEE Commun. Mag.*, vol. 54, no. 5, pp. 36–42, May 2016, doi: 10.1109/MCOM.2016.7470933.

[12] J. Xie, Y. Wan, K. Namuduri, S. Fu, G. L. Peterson, and J. F. Raquet, "Estimation and validation of the 3D smooth-turn mobility model for airborne networks," in *Proc. MILCOM-IEEE Mil. Commun. Conf.*, San Diego, CA, USA, Nov. 2013, pp. 556–561.

[13] J. Xie, Y. Wan, B. Wang, S. Fu, K. Lu, and J. H. Kim, "A comprehensive 3-dimensional random mobility modeling framework for airborne networks," *IEEE Access*, vol. 6, pp. 22849–22862, 2018.

[14] K. U. R. Khan, R. U. Zaman, A. V. Reddy, K. A. Reddy, and T. S. Harsha, "An efficient DSDV routing protocol for wireless mobile ad hoc networks and its performance comparison," in *Proc. 2nd UKSIM Eur. Symp. Comput. Modeling Simulation*, Liverpool, U.K., Sep. 2008, pp. 506–511, doi: 10.1109/EMS.2008.11.

[15] Istikmal, "Analysis and evaluation optimization dynamic source routing (DSR) protocol in mobile adhoc network based on ant algorithm," in *Proc. Int. Conf. Inf. Commun. Technol. (ICoICT)*, Bandung, Indonesia, Mar. 2013, pp. 400–404, doi: 10.1109/ICoICT.2013.6574609.

[16] D. Kumar and S. C. Gupta, "Mobility models and performance of FISHEYE, LANMAR, OLSR and AODV," in *Proc. 10th Int. Conf. Wireless Opt. Commun. Netw. (WOCN)*, Bhopal, India, Jul. 2013, pp. 1–5, doi: 10.1109/WOCN.2013.6616237.

[17] J. Xie, Y. Wan, J. H. Kim, S. Fu, and K. Namuduri, "A survey and analysis of mobility models for airborne networks," *IEEE Commun. Surveys Tuts.*, vol. 16, no. 3, pp. 1221–1238, 3rd Quart., 2014, doi: 10.1109/SURV.2013.111313.00138.

[18] E. Mahdipour, E. Aminian, M. Torabi, and M. Zare, "CBR performance evaluation over AODV and DSDV in RW mobility model," in *Proc. Int. Conf. Comput. Autom. Eng.*, Bangkok, Thailand, Mar. 2009, pp. 238–242, doi: 10.1109/ICCAE.2009.75.

[19] R. Sakaguchi, D. Matsui, R. Nakamura, and H. Ohsaki, "Analysis of constrained random WayPoint mobility model on graph," in *Proc. Int. Conf. Inf. Netw. (ICOIN)*, Barcelona, Spain, Jan. 2020, pp. 312–317, doi: 10.1109/ICOIN48656.2020.9016593.

[20] C. Wang, J. Liu, and J. Kuang, "Performance analysis on direct transmission scheme under RWP mobility model in DTMSNs," in *Proc. 7th Int. Conf. Wireless Commun., Netw. Mobile Comput.*, Wuhan, China, Sep. 2011, pp. 1–4, doi: 10.1109/wicom.2011.6040413.

[21] Y. Gang, "SAR image rapid co-registration based on RD model and coherence interpolation," in *Proc. IEEE Int. Conf. Spatial Data Mining Geographical Knowl. Services*, Fuzhou, China, Jun. 2011, pp. 370–372, doi: 10.1109/ICSDM.2011.5969066.

[22] Y.-T. Liu, J. Xu, and G.-Y. Xia, "Node distribution of the random direction model in a square region," in *Proc. Int. Conf. Mechatronics Control (ICMC)*, Jinzhou, China, Jul. 2014, pp. 21–25, doi: 10.1109/ICMC.2014.7231508.

[23] R. Zhi, F. Gao, and J. Yang, "Nonuniform property of random direction mobility model for MANET," in *Proc. 5th Int. Conf. Wireless Commun., Netw. Mobile Comput.*, Beijing, China, Sep. 2009, pp. 1–4, doi: 10.1109/WICOM.2009.5301659.

[24] Y. Liu, D. Liu, and G. Yue, "BGMM: A body Gauss-Markov based mobility model for body area networks," *Tsinghua Sci. Technol.*, vol. 23, no. 3, pp. 277–287, Jun. 2018.

[25] J.-D.-M. M. Biomo, T. Kunz, and M. St-Hilaire, "An enhanced Gauss-Markov mobility model for simulations of unmanned aerial ad hoc networks," in *Proc. 7th IFIP Wireless Mobile Netw. Conf. (WMNC)*, Vilamoura, Portugal, May 2014, pp. 1–8, doi: 10.1109/WMNC.2014.6878879.

[26] Y. Wang and Y. J. Zhao, "Fundamental issues in systematic design of airborne networks for aviation," in *Proc. IEEE Aerosp. Conf.*, Big Sky, MT, USA, Mar. 2006, p. 8.

[27] M. K. M. Khan and M. S. Rahim, "Performance analysis of social-aware routing protocols in delay tolerant networks," in *Proc. Int. Conf. Comput., Commun., Chem., Mater. Electron. Eng. (IC4ME2)*, Rajshahi, Bangladesh, Feb. 2018, pp. 1–4.

[28] Y. Wan, K. Namuduri, Y. Zhou, and S. Fu, "A smooth-turn mobility model for airborne networks," *IEEE Trans. Veh. Technol.*, vol. 62, no. 7, pp. 3359–3370, Sep. 2013.

[29] D. He, W. Sun, and L. Shi, "The novel mobility models based on spiral line for aerial backbone networks," *IEEE Access*, vol. 8, pp. 11297–11314, 2020, doi: 10.1109/ACCESS.2020.2965616.

[30] W.-J. Hsu, T. Spyropoulos, K. Psounis, and A. Helmy, "Modeling spatial and temporal dependencies of user mobility in wireless mobile networks," *IEEE/ACM Trans. Netw.*, vol. 17, no. 5, pp. 1564–1577, Oct. 2009, doi: 10.1109/TNET.2008.2011128.

[31] O. Erim and C. Wright, "Optimized mobility models for disaster recovery using UAVs," in *Proc. IEEE 28th Annu. Int. Symp. Pers., Indoor, Mobile Radio Commun. (PIMRC)*, Montreal, QC, Canada, Oct. 2017, pp. 1–5, doi: 10.1109/PIMRC.2017.8292716.

[32] J. Ebenezer, "A mobility model for MANET in large scale disaster scenarios," in *Proc. 17th Int. Conf. Comput. Inf. Technol. (ICCIT)*, Dhaka, Bangladesh, Dec. 2014, pp. 59–64, doi: 10.1109/ICCITechn.2014.7073128.

[33] G. Walunjkar and A. K. Rao, "Simulation and evaluation of different mobility models in disaster scenarios," in *Proc. 4th Int. Conf. Recent Trends Electron., Inf., Commun. Technol. (RTEICT)*, Bengaluru, India, May 2019, pp. 464–469, doi: 10.1109/RTEICT46194.2019.9016893.

[34] S. Cabrero, X. G. Paneda, D. Melendi, R. Garcia, and T. Plagemann, "Using firefighter mobility traces to understand ad-hoc networks in wildfires," *IEEE Access*, vol. 6, pp. 1331–1341, 2018, doi: 10.1109/ACCESS.2017.2778347.

[35] N. Chowdhary and P. D. Kaur, "Addressing the characteristics of mobility models in IoV for smart city," in *Proc. Int. Conf. Comput., Commun. Autom. (ICCCA)*, Noida, India, Apr. 2016, pp. 1298–1303, doi: 10.1109/CCAA.2016.7813919.

[36] L. Chettri and R. Bera, "A comprehensive survey on Internet of Things (IoT) toward 5G wireless systems," *IEEE Internet Things J.*, vol. 7, no. 1, pp. 16–32, Jan. 2020, doi: 10.1109/JIOT.2019.2948888.

[37] K. Singh and A. K. Verma, "Experimental analysis of AODV, DSDV and OLSR routing protocol for flying adhoc networks (FANETs)," in *Proc. IEEE Int. Conf. Electr., Comput. Commun. Technol. (ICECCT)*, Coimbatore, India, Mar. 2015, pp. 1–4, doi: 10.1109/ICECCT.2015.7226085.

[38] A. V. Leonov and G. A. Litvinov, "Considering AODV and OLSR routing protocols to traffic monitoring scenario in FANET formed by mini-UAVs," in *Proc. 15th Int. Sci.-Tech. Conf. Actual Problems Electron. Instrum. Eng. (APEIE)*, Novosibirsk, Russia, Oct. 2018, pp. 229–237, doi: 10.1109/APEIE.2018.8545667.

[39] I. U. Khan, I. M. Qureshi, M. A. Aziz, T. A. Cheema, and S. B. H. Shah, "Smart IoT control-based nature inspired energy efficient routing protocol for flying ad hoc network (FANET)," *IEEE Access*, vol. 8, pp. 56371–56378, 2020, doi: 10.1109/ACCESS.2020.2981531.

[40] A. Bujari, C. E. Palazzi, and D. Ronzani, "A comparison of stateless position-based packet routing algorithms for FANETs," *IEEE Trans. Mobile Comput.*, vol. 17, no. 11, pp. 2468–2482, Nov. 2018, doi: 10.1109/TMC.2018.2811490.

[41] J. Zhou, B. Feng, and G. Wei, "A new random mobile model for analysis of ad hoc networks routing protocols," in *Proc. IEEE/IFIP Int. Conf. Embedded Ubiquitous Comput.*, Shanghai, China, Dec. 2008, pp. 711–716.

[42] P. K. Sharma and D. I. Kim, "Coverage probability of 3D UAV networks with RWP mobility-based altitude control," in *Proc. IEEE Int. Conf. Commun. Workshops (ICC Workshops)*, Kansas City, MO, USA, May 2018, pp. 1–6.

[43] P. K. Sharma and D. I. Kim, "Coverage probability of 3-D mobile UAV networks," *IEEE Wireless Commun. Lett.*, vol. 8, no. 1, pp. 97–100, Feb. 2019.

[44] J. P. Rohrer, E. K. Cetinkaya, H. Narra, D. Broyles, K. Peters, and J. P. G. Sterbenz, "AeroRP performance in highly-dynamic airborne networks using 3D Gauss-Markov mobility model," in *Proc.-MILCOM Mil. Commun. Conf.*, Baltimore, MD, USA, Nov. 2011, pp. 834–841.

[45] H. Yun-Hong and X. Yong-Ming, "Reserch on the mechanical-properties of flexible surface-material by erosion in sandstorm-environment," in *Proc. Int. Conf. Mechanic Autom. Control Eng.*, Wuhan, China, Jun. 2010, pp. 3838–3843.

[46] B. Balogh, Z. Illyefalvi-Vitez, G. Kotora, T. Harvey, D. Kirkpatrick, and G. Farmer, "Qualification and reliability tests of flexible printed circuits," in *Proc. 30th Int. Spring Seminar Electron. Technol. (ISSE)*, Cluj-Napoca, Romania, May 2007, pp. 82–87.

[47] B. Gupta and A. Gupta, "On the k-Connectivity of ad-hoc wireless networks," in *Proc. IEEE 7th Int. Symp. Service-Oriented Syst. Eng.*, Redwood City, CA, USA, Mar. 2013, pp. 546–550.

[48] N. M. Freris, H. Kowshik, and P. R. Kumar, "Fundamentals of large sensor networks: Connectivity, capacity, clocks, and computation," *Proc. IEEE*, vol. 98, no. 11, pp. 1828–1846, Nov. 2010.

[49] X. Wang, X. Lin, Q. Wang, and W. Luan, "Mobility increases the connectivity of wireless networks," *IEEE/ACM Trans. Netw.*, vol. 21, no. 2, pp. 440–454, Apr. 2013.

[50] J. Harri, F. Filali, and C. Bonnet, "Mobility models for vehicular ad hoc networks: A survey and taxonomy," *IEEE Commun. Surveys Tuts.*, vol. 11, no. 4, pp. 19–41, 4th Quart., 2009, doi: 10.1109/SURV.2009.090403.

[51] S. A. Dianat, B. Brewington, and L. K. Mestha, "A multidimensional smoothing algorithm with applications to digital color printer calibration," in *Proc. 16th IEEE Int. Conf. Image Process. (ICIP)*, Cairo, Egypt, Nov. 2009, pp. 2025–2028.

[52] S. Lan and Y. Wan, "A non-parametric method for curve smoothing," in *Proc. IEEE 4th Int. Conf. Comput. Commun. (ICCC)*, Chengdu, China, Dec. 2018, pp. 1997–2001.

[53] A. Tiwari, A. Ganguli, and A. Sampath, "Towards a mission planning toolbox for the airborne network: Optimizing ground coverage under connectivity constraints," in *Proc. IEEE Aerosp. Conf.*, Big Sky, MT, USA, Mar. 2008, pp. 1–9.
[54] A. Tiwari, A. Ganguli, A. Sampath, D. S. Anderson, B.-H. Shen, N. Krishnamurthi, J. Yadegar, M. Gerla, and D. Krzysiak, "Mobility aware routing for the airborne network backbone," in *Proc. MILCOM-IEEE Mil. Commun. Conf.*, San Diego, CA, USA, Nov. 2008, pp. 1–7.

DAWEI HE was born in Yanta, Xian, Shannxi, China, in 1992. He received the B.S. degree in communication engineering from the Shannxi University of Technology, Hanzhong, in 2010. He is currently pursuing the M.S. and Ph.D. degrees in aerospace science and technology with Xidian University, College Space, Shannxi.

WEI SUN (Member, IEEE) received the B.S. degree in measuring and control technology and the Ph.D. degree in circuit and system from Xidian University, Xi'an, China, in 2002 and 2009, respectively. He is currently a Professor with the School of Aerospace Science and Technology, Xidian University. His current research interests include multi-UAV systems, visual information perception, pattern recognition, and embedded video systems.

LEI SHI received the B.S. degree in measurement and control and Ph.D. degree in circuits and system from Xidian University, Xi'an, China, in 2006 and 2012, respectively. From 2013 to 2014, he was a Lecturer with the School of Aerospace Science and Technology, Xidian University, where he has been an Associate Professor at the TT&C and Communication Department, since 2015. His research interests include aerospace TT&C and communications, EM propagation, and wireless channel modeling. In particular, a series of groundbreaking studies have been made on the channel modeling and communication methods for hypersonic/reentry vehicles communication.